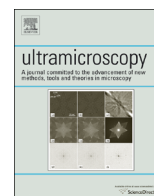




ELSEVIER

Contents lists available at ScienceDirect

Ultramicroscopy

journal homepage: www.elsevier.com/locate/ultramic

Correction of the deterministic part of space–charge interaction in momentum microscopy of charged particles

G. Schönhense^{a,*}, K. Medjanik^a, C. Tusche^b, M. de Loos^c, B. van der Geer^c, M. Scholz^d, F. Hieke^d, N. Gerken^d, J. Kirschner^b, W. Wurth^{d,e}

^a Institut für Physik, Johannes Gutenberg-Universität, 55128 Mainz, Germany

^b Max-Planck-Institut für Mikrostrukturphysik, 06120 Halle, Germany

^c Pulsar Physics, Burghstraat 47, 5614 BC Eindhoven, The Netherlands

^d Physics Department and Center for Free-Electron Laser Science, Univ. Hamburg, 22761 Hamburg, Germany

^e DESY Photon Science, 22607 Hamburg, Germany

ARTICLE INFO

Article history:

Received 19 January 2015

Received in revised form

13 May 2015

Accepted 15 May 2015

Available online 28 May 2015

Keywords:

Momentum microscopy

Space charge

HAXPES

ABSTRACT

Ultrahigh spectral brightness femtosecond XUV and X-ray sources like free electron lasers (FEL) and table-top high harmonics sources (HHG) offer fascinating experimental possibilities for analysis of transient states and ultrafast electron dynamics. For electron spectroscopy experiments using illumination from such sources, the ultrashort high-charge electron bunches experience strong space–charge interactions. The Coulomb interactions between emitted electrons results in large energy shifts and severe broadening of photoemission signals. We propose a method for a substantial reduction of the effect by exploiting the deterministic nature of space–charge interaction. The interaction of a given electron with the average charge density of all surrounding electrons leads to a rotation of the electron distribution in 6D phase space. Momentum microscopy gives direct access to the three momentum coordinates, opening a path for a correction of an essential part of space–charge interaction. In a first experiment with a time-of-flight momentum microscope using synchrotron radiation at BESSY, the rotation in phase space became directly visible. In a separate experiment conducted at FLASH (DESY), the energy shift and broadening of the photoemission signals were quantified. Finally, simulations of a realistic photoemission experiment including space–charge interaction reveals that a gain of an order of magnitude in resolution is possible using the correction technique presented here.

© 2015 Elsevier B.V. All rights reserved.

1. Introduction

The advent of intense pulsed photon and electron sources with pulse lengths in the femtosecond range opened the door to a new generation of experiments targeting ultrafast dynamics and short-lived transient states [1]. On the laboratory scale, numerous table-top devices for the production of ultrashort EUV or X-ray pulses [2] or photocathodes for electron guns [3] have been developed and are currently under development. Free electron lasers (FELs) [4] in particular have emerged as fascinating research tool to study atoms, molecules and solids with a time resolution of a few femtoseconds and a spatial resolution down to the Å range. One key question in condensed matter physics is how complex and often unexpected phenomena emerge from the competing interactions in a quantum many-body system, leading to remarkable

macroscopic phenomena such as high-Tc superconductivity, colossal magnetoresistance and metal–insulator transitions. Time-resolved studies after controlled excitation with light pulses out of equilibrium offer the possibility to identify the most relevant relaxation channels and to potentially gain insight into the driving forces for unexpected ground state properties; for a recent perspective article, see [5].

Photoelectron spectroscopy (PES) is a well-established technique to study the electronic properties; however the information depth is limited to the topmost surface layers. New possibilities for increased depth information come from high-brilliance Synchrotron sources and FELs in the hard X-ray regime. The large mean free path of electrons with kinetic energies above ~5 keV opens access to bulk properties in hard X-ray PES (HAXPES) experiments. Due to the high pulse intensity of such sources, the Coulomb interaction of the particles released within a single short pulse becomes substantial and can result in prohibitively large energy broadenings [6] and a loss of angular- and even of spin

* Corresponding author.

E-mail address: schoenhense@uni-mainz.de (G. Schönhense).

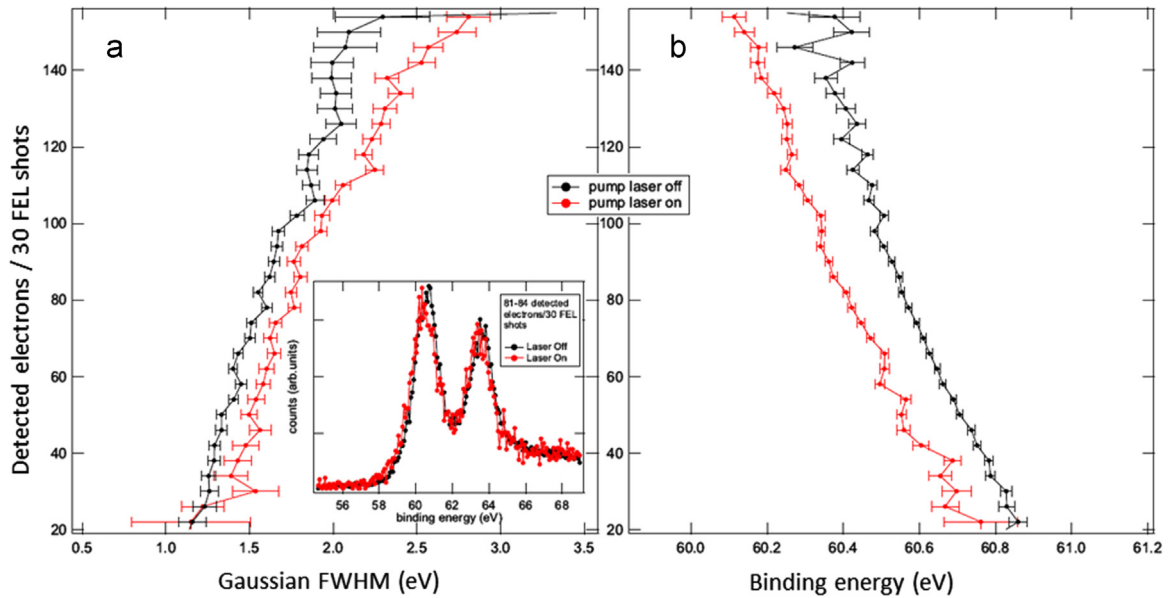


Fig. 1. Space-charge induced broadening (a) and apparent binding energy shift (b) of the Ir $4f_{7/2}$ peak in respect of the number of detected electrons per 30 FEL shots. The measurements were performed at the free-electron laser FLASH at DESY at an excitation energy of 190.7 eV, with (red trace) and without (black trace) a 800 nm optical pump pulse (2.1 mJ/cm^2 , 250 kHz). (For interpretation of the references to color in this figure legend, the reader is referred to the web version of this article.)

information [7]. This is commonly referred to as the *space-charge problem*. As a consequence, electron spectroscopic and imaging methods like angle-resolved photoelectron spectroscopy (ARPES) and photoemission electron microscopy (PEEM) with pulsed sources are facing a dramatic loss in performance.

In common PES, e.g. using hemispherical analyzers or time-of-flight spectrometers being based on the entrance lens optics of such analyzers, the only way a sufficient energy resolution can be achieved is by reducing the photon intensity necessitating an increased acquisition time. The large retardation ratio between the initial kinetic energy, typically $> 5 \text{ keV}$, and pass energy through the analyzer (of the order of a few 100 eV) increases the beam size. In order to cope with the high lateral magnification of the entrance lens (necessary to fulfill Liouville's Theorem) the photon spot on the sample must be of the order of $50 \mu\text{m}$ or less. Repulsive Coulomb forces act during the expansion of the electron cloud in the vicinity of the small probing spot on the sample surface. Once the initial energy and angular distribution is washed out, it cannot be reconstructed and part of the information is lost.

This effect is clearly evident in Fig. 1, which shows data extracted from typical photoemission spectra taken with a hemispherical electron analyzer (Scienta SES 2002) at the free electron laser FLASH at DESY (Hamburg). The $4f_{7/2}$ core-level of an Ir(111) single crystal was studied at an excitation energy of 190.7 eV. The spectra were sorted according to the number of detected electrons in a bunch train of 30 bunches with a separation of $4 \mu\text{s}$ (black error bars, denoting the statistical error). Additionally, we excited the sample with a 2.1 mJ/cm^2 pump laser at 800 nm (red error bars). In this case, we create slow electrons in front of the sample surface by multi-photon excitation. The effect of space-charge induced broadening and apparent binding-energy shift with increasing electron number is clearly visible. The ordinate shows the number of detected electrons, which is proportional to the number of emitted electrons. The space-charge effect (sum of deterministic and stochastic contribution) is enhanced in the presence of the pump laser and hence the presence of a slow electron cloud at the sample surface.

In this paper we describe a method to minimize space-charge induced effects in photoelectron spectroscopy experiments by manipulating the time where Coulomb repulsion between photo-

emitted fast electrons and slow secondary electrons is significant. The influence of the Coulomb interaction on the electron trajectories is minimized by the following means: (i) Accelerating the electrons away from the source region with a high electrostatic field that acts differently on electrons with different energies, (ii) rapid separation of the momentum discs of fast and slow electrons and (iii) exploiting the fact that the deterministic part of the Coulomb interaction originates from the interaction of a given electron with the average charge density of all other electrons.

3D particle tracking techniques have been performed for a monochromatic electron ensemble and for a model distribution of two different electron species (fast electrons model the valence range and slow electrons the secondary cascade). The electric-field distribution in the source region was assumed to have realistic parameters common to electrostatics cathode lenses. Details of the space-charge effect and its spatiotemporal evolution were determined for randomly generated initial bunch charges between 0.1 and 100 fC with spatial and temporal Gauss profiles of $10 \mu\text{m}$ and 30 fs FWHM, respectively (note that Fig. 1 shows only the intensity of the detected electrons being much smaller than the total number or released electrons). The results indicate that the deterministic part can be corrected with a momentum microscope: a cathode-lens type instrument optimized for best resolution in reciprocal space. The simulations reveal a gain of one order of magnitude in spectroscopic performance. The first experiments using synchrotron radiation qualitatively confirm the expected behavior for photon fluxes where the space-charge interaction becomes significant.

2. Momentum microscopy

Momentum microscopy is a novel technique that was developed for detecting the k -distribution of an ensemble of charged particles in a parallel-imaging device. Fig. 2 illustrates the basic principle of such an instrument. Electrons emitted from the sample are accelerated by a strong electrostatic immersion field forming part of the cathode lens (the planar sample surface acting as cathode). The backfocal plane of the objective lens is the image plane for the reciprocal (or Fourier) image. The radial coordinate in

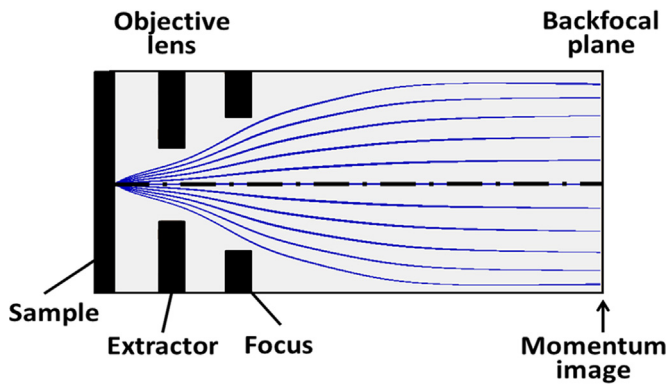


Fig. 2. Basic principle of a momentum microscope. For the high-energy case shown (5 keV start energy), a strong electrostatic field (of the order of 5 MV/m) between sample and extractor leads to an effective collection of rays in a large interval of emission angles. Trajectories were calculated for a real geometry using SIMION 8.1 [10] (electrodes schematic; radial coordinate stretched). The momentum image is located in the backfocal plane of the objective lens; in a real microscope more lenses follow.

this image is a linear measure for the transversal electron momentum k_{\parallel} (parallel to the sample surface). Momentum microscopy aims at utmost resolution of this reciprocal image; recently, a resolution of $5 \times 10^{-3} \text{ \AA}^{-1}$ was demonstrated in an optimized momentum microscope [8]. This value translates into the best angular resolution achieved by hemispherical analyzers. However, unlike for hemispherical analyzers, the momentum resolution stays practically constant with increasing start energy. This is a property of cathode lenses owing to the high extractor field strength.

Since k_{\parallel} is conserved when the electrons escape from the surface, the reciprocal image represents a map of the energy bands in momentum space in terms of the E_B vs k_{\parallel} spectral function (E_B binding energy). For 2D systems (surface states, adsorbate systems, layered materials) this yields the full k_x – k_y momentum information at fixed photon energy. For 3D bulk systems, the photon energy has to be scanned in order to obtain a full tomogram of the 3D bulk Brillouin zone. Characterized by ultimate k_{\parallel} -resolution, simultaneous recording of a large momentum region and an energy resolution in the 10 meV range, momentum microscopy establishes a new route towards angular-resolved PES (ARPES) with utmost detection efficiency.

For low start energies a momentum microscope detects the full half space above the sample surface simultaneously. The cutoff (“photoemission horizon”) is defined by $k_{\parallel}^{\text{max}} = 0.51(E_{\text{kin}})^{1/2}$, with E_{kin} being the kinetic start energy (in eV) and $k_{\parallel}^{\text{max}}$ the parallel momentum at the horizon (in \AA^{-1}). An exemplary discussion of the photoemission horizon can be found in [9]. The existing low-energy instruments are designed for parallel imaging of a momentum range of diameter 6 \AA^{-1} , comprising typically more than the first Brillouin zone. For higher start energies (up to several keV) the lens optics can be modified in order to accept a larger momentum range at the expense of momentum and energy resolution. The trajectories shown in Fig. 2 have been calculated for an optimized high-energy lens (indicated schematically) for a start energy of 5 keV. The rays correspond to a 2D (k_x, k_y) momentum range of diameter 30 \AA^{-1} , establishing an unprecedented detection efficiency in HAXPES.

Fig. 2 shows the cathode lens, i.e. the initial part of the electron-optical column which is the most crucial for the space-charge interaction. In a momentum microscope more lenses follow for zooming in, for electron-optical confinement of the desired source volume, for retardation and for switching between momentum- and real-space imaging (spectroscopic PEEM). Although being optimized for maximum k -resolution, these instruments have also

a good performance in real-space imaging. In k -imaging mode the role of real-space and reciprocal images are reversed. The beam crossovers correspond to Gaussian images. For good k -resolution a small source area is selected by a variable field aperture, placed in an intermediate Gaussian image plane. The magnification in the first Gaussian image is about 14, hence the average electron density is two orders of magnitude lower than in the source volume at the sample surface. Thus the space-charge interaction is weaker in the crossovers as compared to the region just above the source volume at the sample. Hence we restrict our analysis to this most critical region.

A high-performance prototype of momentum microscope has been developed at the Max-Planck Institute of Microstructure Physics, Halle, Germany. This instrument utilizes a *dispersive electron spectrometer* in order to acquire energy cuts through momentum space with excellent energy and momentum resolution (12 meV and $5 \times 10^{-3} \text{ \AA}^{-1}$, respectively) [8]. This instrument is further equipped with an additional imaging spin filter as described in [11,12].

The time-of-flight (ToF) momentum microscope is a joint development of the University of Mainz and the Max-Planck Institute in Halle, in continuation of earlier work on ToF PEEM [13–18]. Implementation of a *ToF section as energy-dispersive element* bears the advantage that photoelectron momentum maps can be taken simultaneously in an energy interval up to several eV width. This is facilitated by a time-resolving image detector [15,19,20] that acquires 3D (k_x, k_y, E_B) data stacks.

Time-of-flight energy discrimination has the potential of very high energy resolution, principally down to the few-meV range [21]. The prototype ToF k -microscope has been operated both using Synchrotron radiation (BESSY II, beamline U125-2 SGM, for first results, see [22]) and using a Ti-sapphire oscillator (80 MHz) in the lab. In the laboratory experiment an energy- and k -resolution of 19 meV and 0.01 \AA^{-1} , respectively, have been reached.

The present project aims at an optimized ToF momentum microscope for the hard X-ray range at the *European XFEL*. With such high-brightness, short pulse-length sources space charge strongly hampers electron spectroscopic experiments. In the next section we will investigate space-charge interactions in a momentum microscope, both by simulation and experiment.

3. Space charge and its spatiotemporal behavior in a momentum microscope

3.1. General considerations

The Coulomb interaction in a beam of charged particles manifests itself in two main contributions (as sketched in Fig. 3a). The *deterministic* part (called “space charge interaction”) originates from the average charge density distribution acting on a given electron. It leads to a rotation of the particle distribution in 6D (x, y, z, k_x, k_y, k_z) phase-space as illustrated in Fig. 3b for one dimension (the local phase-space density is conserved). The second contribution stems from the individual electron–electron scattering processes that are *stochastic* and lead to irreversible “heating” of the beam and thus to a broadening of the distribution (in 6D: increase in phase-space volume). In electron-optical terms, the space-charge interaction leads to an overall diverging force and acts on focal lengths and aberrations of lens systems [23].

Unlike the case of a TEM or SEM, in a photoelectron spectroscopy experiment the energy distribution of the electron ensemble is polychromatic. In PES and PEEM the fastest electrons originate from the region around the Fermi energy ($E_{\text{kin}} = h\nu - \Phi$ with Φ denoting the workfunction), followed by the core-level signals (having less kinetic energy) and finally the large signal of the

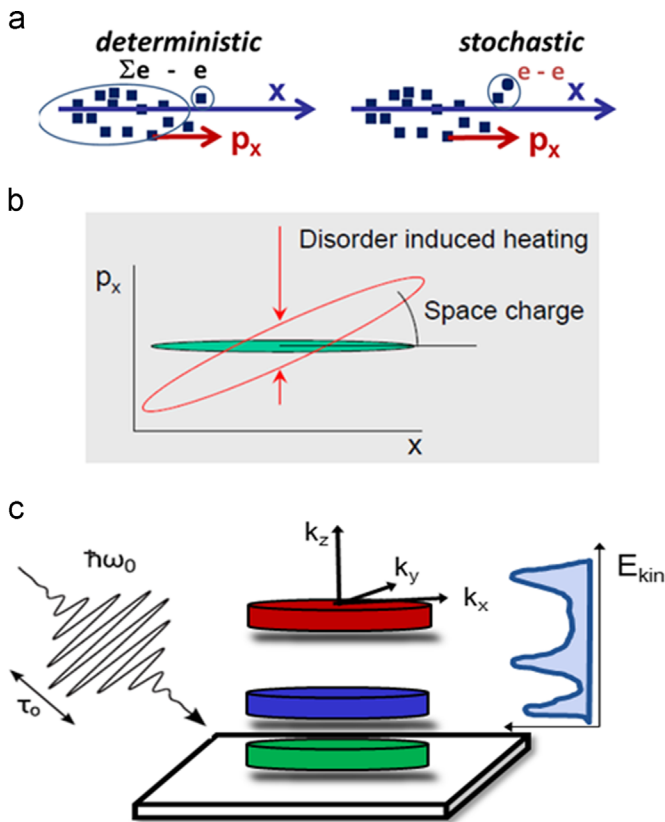


Fig. 3. Deterministic and stochastic part of the Coulomb interaction in real space (a) and phase space (b). In the 1D model example space charge leads to a rotation of the electron distribution in the x - p_x plane. Stochastic heating via e-e collisions leads to a broadening of the distribution (after [26]). For a non-monochromatic energy distribution generated by a short excitation pulse the energy structure leads to a separation into charge clouds as illustrated schematically in (c) for a distribution of three energies.

secondary-electron cascade (eV range). It is worth considering the timescales for the production of these contributions: the main delay between the primary photoemission signal and the slow electrons originates from the thermalization of the non-equilibrium distribution of the inelastically-scattered and secondary electrons. This process lasts up to 100 fs [24]. An additional small contribution results from the different times needed by the fast and slow electrons to travel to the surface; the difference is of the order of 10 fs for an assumed probing depth of about 10 nm in the HAXPES range. Hence, the slow electron signal is slightly delayed and temporally broadened due to the thermalization. After leaving the surface, the ensemble will become spatially structured within some ps after the pulse due to the different starting velocities. In Fig. 3(c) the situation is schematically sketched for an assumed distribution of three different kinetic start energies. The space-charge interaction then leads to acceleration of the fastest and deceleration of the slowest electrons, as discussed in [25]. For fs-excitation, the three discs in (c) are very thin; hence in the representation (b) the ellipse is rather short along x .

3.2. Mono-energetic particle distribution

For the study of the phase-space behavior of an electron ensemble as function of total charge we used the *General Particle Tracer* (GPT) code [26]. This program solves the relativistic equations of motion of a collection of sample particles in realistic fields, including inter-particle Coulomb interactions. All simulation results presented in this paper are obtained with the Particle-In-Cell (PIC) scheme based on an anisotropic multigrid Poisson solver

[27]. The effect of image charges is taken into account with a Dirichlet boundary condition at the $z=0$ plane.

It was verified that granularity effects play an insignificant role by cross-checking the results with GPT's point-to-point model. Due to technical limitations of the point-to-point model this cross-check has been performed where both the point-to-point and the PIC model were run without taking into account the effect of image charges. No significant differences were observed.

In a first run we studied *mono-energetic electrons* with a starting energy of 5 keV, corresponding to the lower end of the HAXPES range. The electrons are launched at $z=0$ and $t=0$ with a random Gaussian temporal profile with 30 fs FWHM. The initial transverse spatial profile is Gaussian with 100 μm FWHM, a realistic value for an X-ray spot behind a refocusing mirror of a synchrotron or FEL monochromator. The total charge Q_{tot} created was varied between 0.1 and 100 fC. For the extractor potential we assumed +50 kV across a gap of 10 mm between grounded sample and extractor (corresponding to a field of 5 MV/m). We simulated the action of the extractor field solely, so the electron trajectories are straight lines in the field-free space behind the extractor. This leads to comparable results for different energies, essentially free of focusing properties of the lenses (except for the weak diverging action of the aperture lens). Coulomb repulsion is significant only in the region close to the sample surface because of the increasing distance between electrons further downstream. For the simulation the extractor plate was mirrored to create an equipotential plane at $z=0$. The opening angle of the random distribution was restricted to $\pm 45^\circ$ to prevent clipping on the hole in the extractor (4 mm).

For each electron of the ensemble launched at $t=0$ the relevant quantities, i.e. the lateral coordinates being proportional to the momentum components k_x and k_y , the energy change ΔE , and the time of flight, are determined in a plane 100 mm behind the sample surface. We will refer to this as the *momentum image*, although in a real microscope more electron lenses are involved. The results are summarized in Fig. 4 showing the total energy spread as function of the total charge created at $t=0$. When increasing the total charge the energy spread also increases from 30 meV at 0.1 fC to 20 eV at 100 fC. The energy spread rises almost *linearly with the amount of charge generated at $t=0$* .

The plots shown as insets give the energy of all electrons in the momentum image versus radial position k_{\parallel} (we term this *point-spread distribution*), color coded on arrival time. We do not quantify the arrival times in this figure; in the prototype time-of-flight momentum microscope (drift section 900 mm) the flight time is $t=600$ ns at a drift energy of $E_D=20$ eV with a dispersion of $\Delta t/\Delta E=10$ ns/eV. For a cylindrically-symmetric initial particle distribution imaged by round lenses, phase space is properly described by the radial and axial coordinates r and z and the radial and axial momentum components k_{\parallel} and k_z . The electron ensembles (insets) are plotted in the $\Delta E(k_{\parallel})$ representation. 10^5 particles were tracked to obtain good statistics, intentionally oversampling the distribution at low charge. Electrons starting parallel to the surface (on the photoemission horizon) leave the cloud most rapidly and thus their Coulomb interaction with the average charge density is much smaller than for electrons traveling along the z -axis. This is the main effect that leads to the tilted distributions in Fig. 4. The rotation described in Fig. 3(a,b) is hidden in the width of the distributions in the insets of Fig. 4, because we cannot resolve the z -coordinate and measure the energy as function of z . Moreover, the initial distribution is very narrow along z , due to the short excitation time of only 30 fs. The inset plots reveal an almost linear dependence between average energy shift and transversal momentum component k_{\parallel} .

In conclusion, the initially mono-energetic electron ensemble experiences a substantial energy spread (total standard deviation)

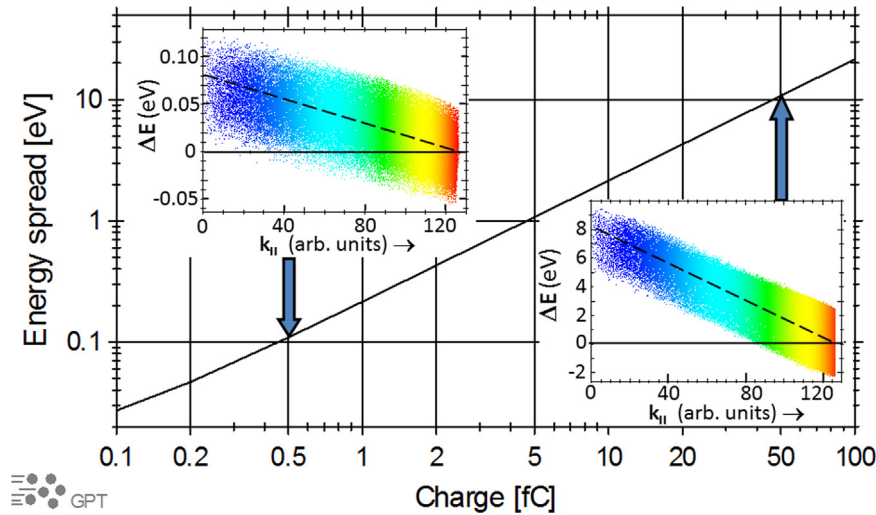


Fig. 4. Summary plot for the energy spread of a single species of fast (5 keV) electrons as function of total charge generated at $t=0$ in Gaussian temporal and spatial beam profiles (widths 30 fs and 100 μm), calculated using the GPT code [26]. Insets: Point-spread distributions for 0.5 fC (left) and 50 fC (right). Particles are color coded on arrival time: blue ones arrive first, red ones arrive last. (For interpretation of the references to color in this figure legend, the reader is referred to the web version of this article.)

of 20 meV, 200 meV, 2 eV and 20 eV for 0.1, 1, 10 and 100 fC, respectively. At 1 fC the spread is of the order of a typical resolution in a HAXPES experiment, the higher values are beyond the tolerable limit for electron spectroscopy in the high-energy range. However, the energy shifts are not statistically distributed in the $\Delta E(k_{||})$ plot. Rather, there is a linear variation of the mean value of the point-spread distribution (denoted by the dashed lines of “best fit”). This variation corresponds to the phase-space rotation discussed above. In the momentum microscope we thus expect an apparent increase of energy which is maximum in the center of the momentum image ($k_{||}=0$) and drops with increasing $k_{||}$ value.

3.3. Refined model of fast electrons and low-energy secondaries

The results for the mono-energetic electron distribution provide a useful guideline for the energy broadening in a diffraction or scattering experiment (e.g. using a small-spot photocathode as source). However, it is unrealistic for a photoemission experiment in the hard X-ray (HAXPES) range. In reality, the signal from the valence band in a HAXPES spectrum is accompanied by the core-level signals and a large background of slow secondary electrons. The intensity of this background rises steeply at small kinetic energies < 5 eV due to the secondary-electron cascade. The cascade exceeds the intensity maximum of the valence bands and core level signals by several orders of magnitude. In this section we will account for this strong signal of cascade electrons in the simulation via a *bimodal* energy distribution. For the fast electron signal we again selected 5 keV in order to directly compare the results with the previous section. We assumed a starting energy of 0.5 eV for the low-energy electrons.

Both particle species emerge within a time interval of 30 fs from the same source spot of 100 μm FWHM with Gaussian distributions in time and space. The spatiotemporal development of this model distribution in the strong immersion lens is at the heart of momentum microscopy. The bimodal distribution was first studied by ray tracing using SIMION 8.1 [10] without space charge. The result is shown in Fig. 5 on the large scale of 80 mm (a) and in detail of the first 1.6 mm in front of the sample surface (b). The different initial velocities show up clearly in the simulation, see time markers with 10 ps spacing in (b). Already after 10 ps the 5 keV electrons are separated by 0.4 mm from the slow electrons which did not move much during this period. After 30 ps the fast

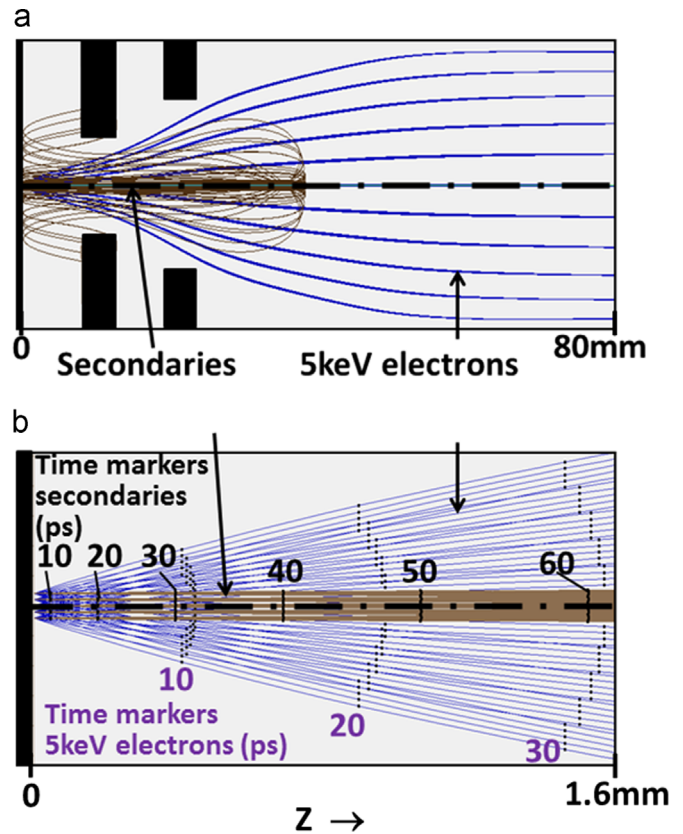


Fig. 5. Spatiotemporal behavior for a model distribution of two electron species, a fast one with 5 keV start energy representing the signal from the valence band and a second one of 0.5 eV modeling the cascade electrons. (a) shows the full distance to the momentum image plane, located 80 mm behind the sample; (b) the first 1.6 mm from the sample surface with time contours every 10 ps (simulated using SIMION). Note the differences in longitudinal and transversal spread of the fast and slow electrons in the strong immersion field.

electrons have reached the right-hand border at 1.6 mm, whereas the slow ones have moved only 0.4 mm. The Coulomb interaction between the fast and slow electrons is already negligible at this distance, i.e. after less than 30 ps.

An eye-catching effect in Fig. 5(b) is the rapid separation of fast and slow electrons in radial direction. Due to the strongly different

transversal momenta of the two species, the expansion of their momentum-distribution discs in the strong extractor field is strikingly different. The 5 keV electrons possess a large transversal momentum of up to 35 \AA^{-1} at the photoemission horizon. As a consequence the high-energy ensemble spreads out rapidly in radial direction. After only 10 ps the electrons of the fast ensemble are sorted by their k_{\parallel} values, i.e. they form an expanding momentum-image disc (lower time markers 10–30 ps in Fig. 5b). In comparison, the transversal momentum of the low-energy ensemble is two orders of magnitude smaller (0.35 \AA^{-1} at the horizon). In the extractor field the slow ensemble thus travels parallel to the optical axis. The resulting pencil beam retains its initial diameter of $100 \mu\text{m}$ FWHM over a long z -distance (upper time markers 10–60 ps in Fig. 5b). We will see below that this rapid radial separation of fast and slow electrons shows up in a systematic change in the phase-space distribution of the fast electron ensemble. Further downstream the retarding potential of the focus electrode repels the cascade electrons completely, as visible in Fig. 5(a).

An assumed electron distribution of this kind with 10% 5 keV electrons and 90% 0.5 eV electrons was simulated in the particle-in-cell model using GPT. A selection of results is shown in Fig. 6. Here the total charge was varied between 1 and 100 fC, equivalent to 6000 to 600,000 electrons in total or 600 to 60,000 in the 5 keV ensemble. Now the situation has changed in comparison to Fig. 4: for a large charge of $Q_{\text{tot}}=100 \text{ fC}$ that led to 20 eV spread for the mono-energetic distribution, the scatter about the dashed curve stays in the $\pm 1 \text{ eV}$ range for large k_{\parallel} (Fig. 6c). For 10 fC total charge, (i.e. 6,000 fast electrons) the distribution at large k_{\parallel} is only $\pm 100 \text{ meV}$ wide. A resolution in the 100 meV range would be very suitable for HAXPES experiments. Without the momentum separation, the total width of this distribution (Fig. 6b) is 1.2 eV, which is prohibitive for HAXPES.

Further calculations revealed that the scattering of the points (rms width) about the dashed lines ($\Delta E(k_{\parallel})$ curve of “best fit”) is defined by the amount of *fast* electrons only. The large background of slow electrons affects the shape and increases the slope of the $\Delta E(k_{\parallel})$ curve but does not increase the rms value.

Fig. 6 reveals several important facts: (i) the $\Delta E(k_{\parallel})$ curves of “best fit” (dashed) are no longer straight as for the mono-energetic distribution (Fig. 4) but get markedly curved with increasing total charge, the slope increases towards $k_{\parallel}=0$; (ii) the rms width of the point-spread distribution around the dashed curves drops with increasing value of k_{\parallel} ; (iii) with increasing total charge the point-spread distribution becomes more and more tilted like in Fig. 4, but now the distributions are a factor of 9 narrower. (iv) the electron density drops towards zero when approaching $k_{\parallel}=0$.

Space-charge correction exploits this tilt of the point-spread distribution in $\Delta E(k_{\parallel})$ representation. The energy corresponding to a counting event at a certain k_{\parallel} is re-normalized to the new zero reference given by the line of “best fit”. For the present set of parameters (Gaussian temporal and spatial beam profiles of widths 30 fs and $100 \mu\text{m}$ FWHM, 10% 5 keV electrons, 90% 0.5 eV electrons, extractor field 5 MV/m) the simulation suggests an increase in energy resolution by one order of magnitude. When the ratio between slow and fast electrons is larger than in our model distribution (which is certainly the case in HAXPES experiments), we expect an even larger gain in resolution. The tilt of the distribution will increase with increasing amount of slow electrons but its rms width will stay essentially constant. For large amounts of slow electrons even the transversal momentum might be increased. However, at the given conditions we did not see indications of this effect, neither in simulations nor in experiment.

The electron density in the momentum image drops significantly towards $k_{\parallel}=0$ and even disappears in the center. The space charge acts similarly as a diverging lens. The repulsion

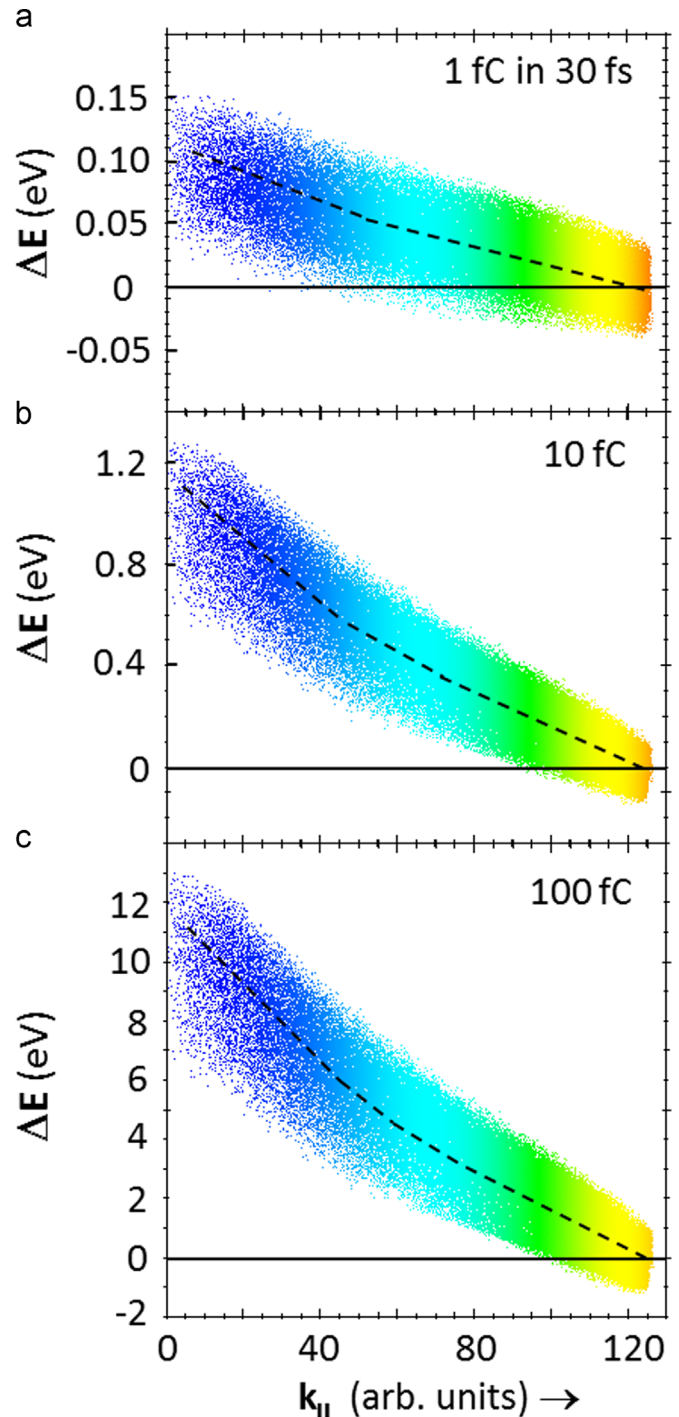


Fig. 6. Point-spread distributions calculated for the case of two electron species (5 keV and 0.5 eV) with intensity ratio *fast:slow* = 1:9. Total charge is 1 fC, 10 fC and 100 fC, only the electrons of the 5 keV ensemble are shown. Dashed lines denote curves of best fit. Blue particles arrive first, red ones arrive last. (For interpretation of the references to color in this figure legend, the reader is referred to the web version of this article.)

between cascade electrons and 5 keV electrons is strongest close to the optical axis because at $k_{\parallel}=0$ their momentum distribution discs interact much longer than the outer part of the rapidly expanding disc of the fast electrons. In HAXPES experiments using a high-energy momentum microscope it might thus be advantageous to concentrate the evaluation on a (ring-shaped) outer region of the momentum image, where the energy spread is lower than in the center region.

Concluding this section, we discuss the behavior in a momentum microscope in comparison with a conventional HAXPES spectrometer. The strong immersion field of the cathode lens causes a spatial confinement of the slow electrons in a thin pencil beam traveling along the optical axis. The average charge density of the large amount of secondary electrons is “point-like”. This confined charge cloud travels along the microscope axis with increasing distance behind the fast electrons. The rapidly expanding momentum disc of the fast electrons interacts in a well-defined way with this confined charge cloud. The Coulomb interaction is always accelerating and is much weaker for electrons with large k_{\parallel} than in the central region. In turn, this leads to a strongly tilted point-spread distribution in the $\Delta E(k_{\parallel})$ representation (Fig. 6c). The spatial separation already happens on a timescale of 10 ps in the accelerating immersion field within a few 100 μm above the sample surface.

In conventional dispersive spectrometers or angle-resolving ToF analyzers there is no rapid k -separation close to the sample. The fast and slow electrons are emitted into the complete half-space above the sample surface. The lens fields start to act far away from the surface, where the mixed ensemble of different energies has spread due to their different velocities, like illustrated in Fig. 3c. Hence the space charge interaction occurs (equally) at all take-off angles. In the immersion lens the point-like charge cloud of slow electrons is effectively kept away from the outward-dispersing fast electrons. The space-charge effect at large k_{\parallel} therefore becomes small, and the outer ring-shaped region in the momentum image can be directly used to evaluate high-resolution energy spectra without further correction. This is not the case for conventional hemispherical analyzers.

3.4. Experimental results

The essential predictions of Fig. 6, namely the acceleration of the electrons near the center of the beam and the drop of the kinetic energy with increasing parallel momentum were investigated using the ToF momentum microscope at the synchrotron source BESSY, see Fig. 7. The parameters were: photon energy 35 eV, single bunch (1.25 MHz repetition frequency), photon flux about 3×10^{10} photons/s, sample Mo(110), extractor potential 10 kV, pass energy of drift section 20 eV. The patterns show a surface state arising in a partial bandgap of Mo [22] taken at a temperature of 140 K.

The two energy-vs-momentum sections (a) and (b) have been taken at photon fluxes differing by about one order of magnitude as estimated from the count rates. The pattern at lower flux (a) exhibits a sharp, straight cutoff at maximum energy, corresponding to the Fermi edge E_F . At the higher photon flux (b) a

marked curvature of the Fermi cutoff is obvious. The energy shift reaches its maximum of 0.4 eV on the axis ($k_{\parallel}=0$) and drops to both sides with increasing k_{\parallel} , as predicted by the simulations. The band features close to $k_{\parallel}=0$ are lifted in energy by the same amount, the high-intensity point at $k_{\parallel}=0$ is marked by a circle. In addition, all features are smeared out in panel (b) due to the e–e scattering processes.

Being taken at a kinetic start energy of 30 eV, this result cannot be quantitatively compared with the simulations for 5 keV. At the Fermi cutoff the start velocity is a factor of 13 smaller than in the simulation, i.e. closer to the velocity of the secondary electrons. The extractor field was also lower than the one assumed for the simulations. Hence, the experimental result lies in between the limiting cases of Figs. 4 and 6. The principal behavior agrees with the theoretical predictions.

4. Summary and conclusion

Photoelectron spectroscopy using fs pulsed sources like free-electron lasers or table-top high harmonic sources is presently developing into a new tool targeting ultrafast dynamics and short-lived transient states. Exciting possibilities towards increased depth information come along with high-brilliance synchrotron sources and FELs in the hard X-ray regime (like the European XFEL). Due to the high pulse intensity of such sources, the Coulomb interaction of the electrons released within a few fs becomes substantial, resulting in energy broadenings and shifts that can mask the transient electronic effects. Photoemission experiments at such sources need optimized strategies for efficient electron detection and for minimization of the space-charge effect. In this article we have presented results of a feasibility study focusing on the question whether momentum microscopy is an appropriate tool to cope with these challenges and to correct part of the space-charge problem.

The study is based on electron trajectory calculations and simulations of the space-charge effect for the model geometry of a cathode-lens optimized for large starting energies. Simulations were performed for a mono-energetic distribution with 5 keV initial energy and for a bimodal distribution (10% 5 keV electrons and 90% 0.5 eV electrons, modeling the secondary cascade). Electron distributions were launched at $t=0$, assuming random Gaussian profiles in space and time (100 μm and 30 fs FWHM, respectively). The space-charge effect was calculated for total charges between 0.1 and 100 fC, using the *General Particle Tracer* (GPT) code [26]. Corresponding electron trajectories in the limit of negligible space-charge interaction were calculated using *SIMION* [10]. The high starting energy was accounted for by an extractor

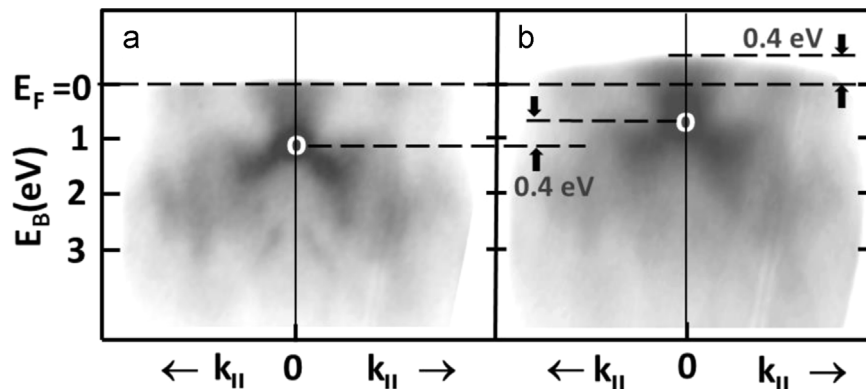


Fig. 7. Energy-vs-momentum sections for a Mo(110) sample measured in a ToF momentum microscope at a photon energy of 35 eV and a temperature of 140 K. Panel (b) was measured for the same settings as (a) but with about an order of magnitude higher photon flux. The space-charge interaction leads to a k_{\parallel} -dependent increase of the energy of the valence electrons, visible in a bulging of the Fermi cutoff and a rising of the point denoted by the circle by the same amount.

field of 5 MV/m (anode potential of +50 kV across a gap of 12 mm). Coulomb interaction manifests itself in terms of two contributions: the *deterministic part* is the interaction of an electron with the combined charge density of all others, also termed space-charge interaction. It leads to a generalized rotation of the electron distribution in 6D phase space. The *stochastic part* represents the e–e scattering processes that lead to irreversible heating of the beam, visible in an increase of the energy spread.

The results can be summarized as follows: an optimized cathode-lens type instrument is well suited for parallel imaging of the momentum distribution of electrons in the energy range of several keV and a k -range of about 30 \AA^{-1} . The simulations were focused on the question, how the space-charge interaction shows up in the momentum images and how the large signal of secondary electrons contributes to the Coulomb interactions. The momentum disc of the 5 keV electrons expands rapidly and after only 10 ps the electrons are spatially separated according to their k_{\parallel} values. Fast electrons with large k_{\parallel} leave the initial ensemble within ~ 10 ps and thus experience much less Coulomb interaction with the average charge density than electrons traveling close to the axis. This leads to a systematic, k_{\parallel} -dependent energy shift ΔE that is already visible for the mono-energetic distribution (insets in Fig. 4). The extractor field effectively separates the momentum-distribution discs of fast and slow electrons: due to their negligible transversal momentum component the latter are confined to a “point-like” charge cloud by the strong electrostatic immersion field. The accelerating effect of this charge cloud on the expanding momentum disc of the fast electrons is at its maximum on axis and drops with increasing k_{\parallel} . The width of the point-spread distribution of the fast electrons stays essentially the same as for the mono-energetic case of the same charge. However, the slope of the “best-fit” function $\Delta E(k_{\parallel})$ becomes steeper at small k_{\parallel} -values (dashed line in Fig. 6c). This effect does not exist in conventional hard X-ray photoemission experiments using hemispherical analyzers, because in the region above the sample surface the slow and fast electrons are emitted into the full half space and are separated only by their different velocities. Giving access to the relevant phase-space coordinates, a momentum microscope opens the door to a correction of the space-charge effect, utilizing the empirical function $\Delta E(k_{\parallel})$.

The theoretical results are qualitatively confirmed by experimental data for the low-energy range ($h\nu = 35 \text{ eV}$), taken with the novel time-of-flight momentum microscope during its first synchrotron beamtime (BESSY, Berlin; single bunch operation at 1.25 MHz, see [22]). With increasing photon flux a marked curvature (bulging) of the formerly straight Fermi cutoff occurred, with an energy increase of up to 0.4 eV at $k_{\parallel} = 0$ and continuous drop with increasing k_{\parallel} (Fig. 7). As predicted by the simulations, the band features close to $k_{\parallel} = 0$ are lifted in energy by the same amount and are smeared out due to the e–e scattering.

In conclusion, we propose momentum microscopy as a powerful new method for photoelectron spectroscopy in the hard X-ray range. Using a lens with enlarged gap and high extractor potential, (k_x, k_y) momentum discs with diameters up to 30 \AA^{-1} can be detected simultaneously. This large acceptance in k -space along with parallel energy acquisition using the ToF approach promises unprecedented performance as a HAXPES spectrometer. In the low-energy experiment [22], about 10^6 $(k_x, k_y, E_{\text{kin}})$ data voxels were acquired simultaneously without any sweeping of potentials or sample rotation. Owing to its deterministic nature, the space-charge part of the Coulomb interaction can be corrected in the momentum distributions. For this, the measured kinetic energies are re-normalized by taking the tilt and curvature of the $E(k_{\parallel})$ -distribution into account, i.e. the energy values are referenced to the lines of “best fit” (dashed curves in Figs. 4 and 6). For the assumed parameter set the *GPT* calculation predicts a gain in

energy-resolution by an order of magnitude. Last but not least, the results are important for new strategies of beam correction via further development towards dynamic aberration correction as discussed previously [28,29].

The performance of momentum microscopes and conventional spectrometers is principally limited by the particle detector. Finally, we mention a current development of a multi-anode design for the 3D $(k_x, k_y, E_{\text{kin}})$ -resolving delay-line detector (DLD). The 4-quadrant DLD [30] has set the remarkable record of burst rates above 100 Mcps and permanent randomly measured 40 Mcps; a 16-segment prototype was tested in a pilot experiment at the free-electron laser FLASH [31]. Striving for even higher integration, 128- and 256-segment DLD solutions are developed in a cooperation of W. Wurth et al. with Surface Concept GmbH and for the SQS photon spectrometer at the European XFEL [32].

Acknowledgments

We acknowledge cooperation and fruitful discussions with many colleagues on various aspects of momentum microscopy, electron spectroscopy and the space-charge problem. Thanks are due to Hans-Joachim Elmers, Sergey Chernov, Dmitro Kutnyakhov, Andreas Oelsner, Ruud Tromp, Oliver Schaff, Yves Acremann, Andrei Gloskowski, Edgar Vredenbrecht and Daniel Comparat. We are grateful to the BESSY staff (in particular C. Schüssler and A. Föhlisch) for support during the beamtime and to Andrew McCulloch for a critical reading of the manuscript. The project is funded by BMBF, Germany (05K13UM2 (Mainz), 05K12EF1 (Halle) and 05K13GU3 (Hamburg) within the priority program FSP 302-FEL) and Center of Innovative Materials Mainz (CINEMA).

References

- [1] F. Krausz, M. Ivanov, *Rev. Mod. Phys.* 81 (2009) 163.
- [2] A. Rundquist, C.G. Durfee III, Z. Chang, C. Herne, S. Backus, M.M. Murnane, H. C. Kapteyn, *Science* 280 (1998) 5368.
- [3] B.J. Siwick, J.R. Dwyer, R.E. Jordan, R.J.D. Miller, *Science* 302 (2003) 1382.
- [4] (a) W. Ackermann, et al., *Nat. Photonics* 1 (2007) 336;
(b) B.W.J. McNeil, N.R. Thompson, *Nat. Photonics* 4 (2010) 814.
- [5] H. Petek, *ACS Nano* 8 (2014) 5.
- [6] A. Pietzsch, et al., *N. J. Phys.* 10 (2008) 033004.
- [7] A. Fognini, et al., *N. J. Phys.* 16 (2014) 043031.
- [8] C. Tusche, A. Krasnyuk, J. Kirschner, *Ultramicroscopy* 159 (p3) (2015) 520.
- [9] A. Winkelmann, A.A. Ünal, C. Tusche, M. Ellguth, C.-T. Chiang, J. Kirschner, *N. J. Phys.* 14 (2012) 083027.
- [10] D.A. Dahl, *Int. J. Mass Spectrom.* 200 (2000) 3.
- [11] C. Tusche, M. Ellguth, A.A. Ünal, C.-T. Chiang, A. Winkelmann, A. Krasnyuk, M. Hahn, G. Schönhense, J. Kirschner, *Appl. Phys. Lett.* 99 (2011) 032505.
- [12] D. Vasilyev, C. Tusche, F. Giebels, H. Gollisch, R. Feder, J. Kirschner, *J. Electron Spectrosc. Relat. Phenom.* 199 (2015) 10.
- [13] H. Spiecker, O. Schmidt, Ch. Zietzen, D. Menke, U. Kleineberg, R.G. Ahuja, M. Merkel, U. Heinzmann, G. Schönhense, *Nucl. Instrum. Meth. A* 406 (1998) 499.
- [14] G. Schönhense, A. Oelsner, O. Schmidt, G.H. Fecher, V. Mergel, O. Jagutzki, H. Schmidt-Böcking, *Surf. Sci.* 480 (2001) 180.
- [15] A. Oelsner, O. Schmidt, M. Schicketanz, M.J. Klais, G. Schönhense, V. Mergel, O. Jagutzki, H. Schmidt-Böcking, *Rev. Sci. Instrum.* 72 (2001) 3968.
- [16] M. Cinchetti, A. Oelsner, G.H. Fecher, H.J. Elmers, G. Schönhense, *Appl. Phys. Lett.* 83 (2003) 1503.
- [17] A. Gloskowski, S.A. Nepijko, M. Cinchetti, G. Schönhense, G.H. Fecher, H. C. Kandpal, C. Felser, H.A. Therese, N. Zink, W. Tremel, A. Oelsner, *J. Appl. Phys.* 100 (2006) 084330.
- [18] G. Schönhense, H.J. Elmers, S.A. Nepijko, C.M. Schneider, *Adv. Imaging Electron Phys.* (2006) 159.
- [19] A. Oelsner, et al., *J. Electron Spectrosc. Relat. Phenom.* 178–179 (2010) 317.
(www.surface-concept.com).
- [20] U. Becker, B. Langer, *Nucl. Instrum. Meth. A* 501 (2009) 78.
- [21] S. Chernov, K. Medjanik, C. Tusche, D. Kutnyakhov, S.A. Nepijko, A. Oelsner, J. Braun, J. Minár, S. Borek, H. Ebert, H.-J. Elmers, J. Kirschner, G. Schönhense, *Ultramicroscopy* 159 (p3) (2015) 453.
- [22] P.W. Hawkes, E. Kasper, *Principles of Electron Optics*, Elsevier, 1996, ISBN: 978-0-12-333340-7.
- [24] N. Medvedev, U. Zastra, E. Förster, D.O. Gericke, B. Rethfeld, *Phys. Rev. Lett.*

- 107 (2014) 165003.
- [25] M. Dell'Angela, T. Anniyev, M. Beye, R. Coffee, A. Föhlisch, J. Gladh, S. Kaya, T. Katayama, O. Krupin, A. Nilsson, D. Nordlund, W.F. Schlotter, J.A. Sellberg, F. Sorgenfrei, J.J. Turner, H. Ostrom, H. Ogasawara, M. Wolf, W. Wurth, *Struct. Dyn.* 2 (2015) 025101.
- [26] S.B. van der Geer, O.J. Luiten, M.J. de Loos, G. Pöplau, U. van Rienen, *Inst. Phys. Conf. Ser.* 175 (2005) 101.
- [27] G. Pöplau, U. van Rienen, S.B. van der Geer, M.J. de Loos, *IEEE Trans. Magn.* 40 (2004) 714.
- [28] G. Schönhense, H. Spiecker, *J. Vac. Sci. Technol. B* 20 (2002) 2526, US Patent 6,737,647 B2 and German Patent DE 102 17 507 B4.
- [29] G. Schönhense, H.J. Elmers, *Surf. Interface Anal.* 38 (2006) 1578.
- [30] German patent DE10335718 B4.
- [31] A. Oelsner, P. Lushchik, D. Kutnyakhov, A. Fognini, D. Perriard, G. Salvatella, C. Stieger, R. Gort, T. Bähler, T. Michlmayer, W. Wurth, Y. Acremann, A. Vaterlaus, G. Schönhense, 2015 (in preparation).
- [32] M. Turcato, P. Gessler, S. Hauf, M. Kuster, M. Meyer, J. Nordgren, J. Sztuk-Dambietz, C. Youngman, *J. Instrum.* 9 (2014) C05063, <http://dx.doi.org/10.1088/1748-0221/9/05>.